Monthly Notices of the ROYAL ASTRONOMICAL SOCIETY

MNRAS **547,** 1–11 (2026) https://doi.org/10.1093/mnras/stag328
Advance Access publication 2026 February 17

A milli-tidal disruption event model for GRB 250702B: main-sequence star disrupted by an IMBH

Jonathan Granot [1,2,3★] Hagai B. Perets [2,4★] Ramandeep Gill [2,5★] Paz Beniamini[1,2,3] and Brendan O'Connor[6†]

[1]*Department of Natural Sciences, The Open University of Israel, P.O Box 808, Ra'anana 4353701, Israel*
[2]*Astrophysics Research Center of the Open University (ARCO), The Open University of Israel, P.O Box 808, Ra'anana 43537, Israel*
[3]*Department of Physics, The George Washington University, 725 21st Street NW., Washington, DC 20052, USA*
[4]*Department of Physics, Technion – Israel Institute of Technology, Haifa 3200002, Israel*
[5]*Instituto de Radioastronomía y Astrofísica, Universidad Nacional Autónoma de México, Antigua Carretera a Pátzcuaro # 8701, Ex-Hda. San José de la Huerta, Morelia, Michoacán C.P. 58089, México*
[6]*McWilliams Center for Cosmology and Astrophysics, Department of Physics, Carnegie Mellon University, Pittsburgh, PA 15213, USA*

Accepted 2026 February 12. Received 2026 February 11; in original form 2025 December 17

ABSTRACT

GRB 250702B is the longest gamma-ray burst (GRB) recorded so far, with multiple gamma-ray emission episodes spread over a duration exceeding 25 ks and a weaker soft X-ray pre-peak ~ 1 day gradually rising emission. It is offset from its host galaxy centre by ~ 5.7 kpc, and displays a long-lived afterglow emission in radio to X-ray. Its true nature is unclear, with the two leading candidate classes of objects being a peculiar type of ultralong GRB and a tidal disruption event (TDE) by an intermediate mass black hole (IMBH). Here, we consider the latter, mTDE origin. We model the afterglow data, finding a stratified external density profile $\propto r^{-k}$ with $k = 1.60 \pm 0.17$, consistent with Bondi accretion of the interstellar medium (of initial number density $n_{\rm ISM} = n_0\,{\rm cm}^{-3}$ and sound speed $c_s = c_{s,6}10^6\,{\rm cm\,s}^{-1}$) for which $n(r) \approx n_{\rm ISM}(r/R_{\rm B})^{-3/2}$ within the Bondi radius $R_{\rm B}$. Moreover, we use the implied density normalization to infer the IMBH mass within this model, finding $M_\bullet \approx \left(6.55^{+3.51}_{-2.29}\right) \times 10^3\, n_0^{-2/3}\, c_{s,6}^2 (1+\mathcal{M}^2)\,{\rm M}_\odot$ where $\mathcal{M} \equiv v_{\rm BH}/c_s$ is the IMBH's Mach number relative to the ISM. Together with an upper limit on $M_\bullet < \frac{c^3}{G}\frac{t_{\rm MV}}{1+z} \lesssim 5 \times 10^4\,{\rm M}_\odot$ from the source-frame minimum variability time $t_{\rm MV,src} = \frac{t_{\rm MV}}{1+z} \approx 0.5$ s this implies $v_{\rm BH} \lesssim 28\, n_0^{1/3}\,{\rm km\,s}^{-1}$. We show that an mTDE of a main-sequence star (but not of a white dwarf) can explain the duration and energetics of GRB 250702B. The gradual rise to the peak may be caused by gradual circularization and accretion disc buildup, leading to an increase in the jet's power and Lorentz factor.

Key words: accretion, accretion discs – stars: black holes – gamma-ray burst: general – ISM: jets and outflows.

1 INTRODUCTION

The unique event GRB 250702B was detected by several different instruments onboard different satellites, including the *Fermi* Gamma-ray Burst Monitor (GBM; E. Neights et al. 2025b, c), the *Space Variable Objects Monitor* (*SVOM*; J. Wei et al. 2016), the *Neil Gehrels Swift Observatory* (N. Gehrels et al. 2004), the *Monitor of All-sky X-ray Image* (*MAXI*; Y. Kawakubo et al. 2025), Konus-Wind (D. Frederiks et al. 2025), and the *Einstein Probe* (EP; H. Q. Cheng et al. 2025). Its main (or prompt) emission episode caused multiple *Fermi*-GBM triggers that were initially catalogued as separate GRBs (e.g. GRB 250702B/D/E; E. Neights et al. 2025a), but were later recognized to originate from the same sky location and are now collectively referred to as GRB 250702B (A. J. Levan et al. 2025).

The prompt emission phase had a duration of $T_{90} \sim 25$ ks, the longest for any GRB, and it showed short time-scale variability, with minimal variability times $t_{\rm MV} \sim 1{-}10$ s in different time intervals (E. Neights et al. 2025a). It was also preceded by a soft X-ray (0.5–4 keV) gradually rising pre-peak emission that was discovered by EP (H. Q. Cheng et al. 2025; D. Y. Li et al. 2025) and started about a day before the first trigger. The main emission episode was followed by a longer-lived emission in radio (K. D. Alexander et al. 2025; P. Atri et al. 2025; A. Balasubramanian et al. 2025; N. Grollimund et al. 2025; A. I. Sfaradi et al. 2025; A. J. Tetarenko et al. 2025), infrared (J. Carney et al. 2025), and X-ray (B. O'Connor et al. 2025, and references therein). The radio, infrared, and late (> 3 d) X-ray emission are consistent with an afterglow origin, from a forward external shock propagating into the external medium, which was powered by a relativistic jet launched by the source (e.g. J. Carney et al. 2025; A. J. Levan et al. 2025; B. O'Connor et al. 2025). However, the early (< 3 d) X-ray emission shows significant short time-scale variability (with $\Delta t/t$ as low as $\sim 10^{-2.5}$) including sharp large-amplitude dips in the flux (B. O'Connor et al. 2025), which exclude an afterglow

★ E-mail: granot@openu.ac.il (JG); hperets@ph.technion.ac.il (HBP); r.gill@irya.unam.mx (RG)
† McWilliams Fellow.

origin of the early-time (< 3 d) X-ray emission, which instead likely arise from internal dissipation in a relativistic collimated outflow driven by late time accretion on to the central source.

The EP detection provided arcminute localization, which allowed the *Swift*-XRT detection that led to arcsecond localization (J. A. Kennea et al. 2025). This in turn allowed near-infrared (NIR) observation and detection by the Very Large Telescope (VLT; A. J. Levan et al. 2025), followed by *Hubble Space Telescope* (*HST*) observations that revealed an irregular host galaxy with the source offset from its centre by ∼0.7 arcsec (A. J. Levan et al. 2025). An observation with the *James Webb Space Telescope* (B. P. Gompertz et al. 2025) led to a host galaxy spectroscopic redshift of $z = 1.036$, which implies a projected source offset from the galaxy centre of ~ 5.7 kpc (J. Carney et al. 2025) and an isotropic equivalent gamma-ray energy of $E_{\gamma,\rm iso} \gtrsim 1.4 \times 10^{54}$ erg (E. Neights et al. 2025a). The soft X-ray pre-peak gradually rising EP emission had an isotropic equivalent energy of $E_{X,\rm iso} \gtrsim 10^{52}$ erg (H. Q. Cheng et al. 2025; D. Y. Li et al. 2025), and was likely beamed, although possibly less so than the main peak.

There is a very large dust extinction towards this source, both from our Galaxy ($A_{\rm V} = 0.847$ mag; E. F. Schlafly & D. P. Finkbeiner 2011) and from within its host galaxy ($A_{\rm V,z} > 5$ mag; J. Carney et al. 2025; B. P. Gompertz et al. 2025; A. J. Levan et al. 2025; B. O'Connor et al. 2025). Together with the fairly high redshift, this would make it very difficult to detect any associated supernova, even if it was present and intrinsically luminous.

A scenario involving a stellar mass black hole is possible, and may naturally produce the very short minimal variability time, $t_{\rm MV}$ as low as ~ 1 s. In particular many of the properties of GRB 250702B are consistent with the long end of the ultralong GRB population (e.g. Y. Y. Tikhomirova & B. E. Stern 2005; B. Gendre et al. 2013; A. J. Levan et al. 2014; M. Boër, B. Gendre & G. Stratta 2015; J. Greiner et al. 2015; B. Gendre 2025), whose origin is still unclear.

Prolonging engine activity to $\sim 10^4$–10^5 s in collapsar-like models typically requires either finely tuned fallback envelopes or sustained accretion from a residual torus, and even then reproducing a smooth day-scale, gradually rising soft X-ray component preceding the main peak is challenging, since the jet must first drill through the stellar envelope while its power is still ramping up.

An alternative scenario featuring a tidal disruption event (TDE) by a stellar-mass black hole, dubbed micro-TDE or μTDE, was suggested as the origin of ultralong GRBs (H. B. Perets et al. 2016), and is explored in detail as the origin of GRB 250702B in P. Beniamini, H. B. Perets & J. Granot (2025). White-dwarf – intermediate mass black hole (IMBH) tidal disruption events have also been suggested as a possible origin for GRB 250702B and other ultralong GRBs (e.g. R. A. Eyles-Ferris et al. 2025; D. Y. Li et al. 2025), however, as we also discuss below, this scenario is significantly challenged if not excluded.

The significant offset from the host galaxy's centre, along with the very short minimal variability time, strongly disfavours a regular TDE, caused by a supermassive black hole (SMBH). However, a TDE caused by an IMBH, i.e. a milli-TDE or mTDE, is still possible and is the scenario we study in this work. In particular, it is consistent with the ~ 5.7 kpc offset from the host galaxy centre (J. Carney et al. 2025). Moreover, it may also accommodate the very short source frame minimal variability time, $\frac{t_{\rm MV}}{1+z} \sim 0.5$–$5$ s (E. Neights et al. 2025a). A robust lower bound on significant variability of the high luminosity emission may be set by r_g/c, which in turn implies an upper limit of $M_\bullet < \frac{c^3}{G}\frac{t_{\rm MV}}{1+z} \lesssim 5 \times 10^4\,{\rm M}_\odot$ on the IMBH mass in a mTDE scenario (see also B. O'Connor et al. 2025).

In § 2, we perform a fit to the GRB 250702B afterglow data, showing that the external density profile is consistent with a stratified external density profile expected for Bondi accretion. In § 3, we use the external density normalization derived in § 2 to infer the IMBH mass in a mTDE scenario (§ 3.1) and consider different possible IMBH environments (§ 3.2). In § 4, we discuss how a mTDE scenario can explain the time-scales and energetics of the soft X-ray pre-peak emission (attributed to circularization, accretion disc buildup, and relativistic jet launching) and of the main emission (attributed to a fully developed accretion-powered jet). In § 5, we discuss our conclusions.

2 AFTERGLOW MODELLING

Here, we fit the radio, infrared, and late (> 3 d) X-ray data (for the data compilation, see J. Carney et al. 2025; A. J. Levan et al. 2025; B. O'Connor et al. 2025) to a standard afterglow model from R. Gill & J. Granot (2023), which is based on many previous works (e.g. R. Blandford & C. McKee 1976; R. Sari & T. Piran 1995; R. Sari, T. Piran & R. Narayan 1998; S. Kobayashi & R. Sari 2000; J. Granot & R. Sari 2002; S. Kobayashi & B. Zhang 2003; J. Granot 2005, 2012; L. Nava et al. 2013; R. Gill & J. Granot 2018; P. Beniamini, J. Granot & R. Gill 2020; P. Beniamini, R. Gill & J. Granot 2022). This model assumes a uniform narrow jet of half-opening angle θ_j, isotropic equivalent kinetic energy $E_{\rm k,iso}$, initial Lorentz factor $\Gamma_0 \geq \theta_j^{-1}$, a power-law external mass density $n(r) = n_d(r/R_d)^{-k}$ with pivot radius $R_d = 10^{18}$ cm (at which the density normalization is fit, and is hence chosen such that significant observed emission arises from its vicinity) and density normalization $n_d = n_{0,d}\,{\rm cm}^{-3}$. It considers the joint dynamics of both the forward shock (FS) that propagates ahead of the ejecta into the external medium, as well as the reverse shock (RS) that propagates through the ejecta, to calculate the dynamical evolution of the contact discontinuity separating the two shocked regions (for further details see R. Gill & J. Granot 2023). Synchrotron radiation from the shocked material behind the two shocks is calculated using the standard afterglow theory that assumes a fraction, ϵ_B, of the internal energy in magnetic fields and a fraction, ϵ_e, in relativistic electrons with a power-law energy distribution with index p. The same quantities for the reverse shock are shown with a subscript 'RS'. Observations were corrected for extinction ($A_{\rm V}$) and photoelectric absorption ($N_{\rm H}$) from within our galaxy, where the latter was also accounted for in the host galaxy (see B. O'Connor et al. 2025). The afterglow fit separately accounts for extinction intrinsic to the host galaxy or local environment of the source. Fig. 1 shows the Markov chain Monte Carlo (MCMC) fit to the multiwavelength observations, where the light curves are obtained for the best-fitting parameters as shown in the posterior distributions of parameters in Fig. A1. The X-ray and NIR light curves are completely explained by emission from the FS. The radio light curves, on the other hand, receive some contribution from the RS emission that produces the mild bump at times $t \sim 10^5$–10^6 s. Overall, the model light curves are consistent with observations. The MCMC posteriors (Fig. A1) show that, although there are the usual degeneracies between $E_{\rm k,iso}$, n_d, and the microphysical parameters, the external density slope k is relatively well constrained and prefers a stratified profile ($k = 1.60 \pm 0.17$) over a uniform medium ($k = 0$). Values $0 < k < 2$ are also commonly

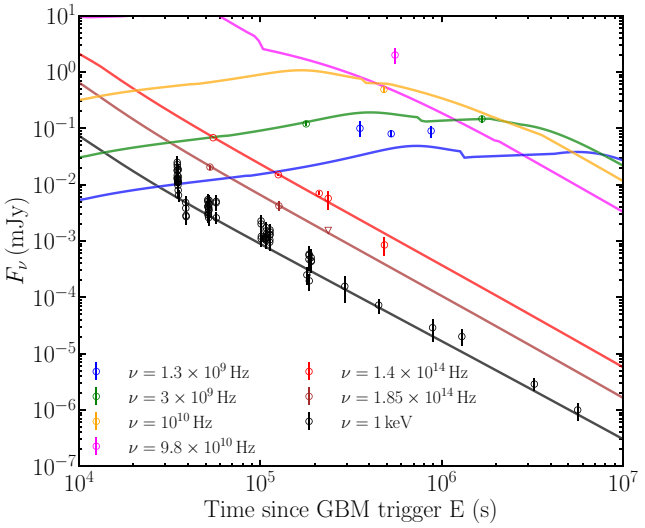

Figure 1. Best-fitting model light curve obtained from an MCMC fit to the multiwavelength afterglow data of GRB 250702B. The model parameter posterior distributions are shown in Fig. A1. The bump in the radio light curves at $10^5\,\mathrm{s} \lesssim t \lesssim 10^6\,\mathrm{s}$ is produced by a contribution from the reverse shock emission.

inferred for long GRBs with well-monitored afterglows (e.g. C. Kouveliotou et al. 2013; E.-W. Liang et al. 2013; B. P. Gompertz, A. S. Fruchter & A. Pe'er 2018; Q.-Q. Zhou et al. 2020), so this result by itself does not rule out collapsar-like progenitors. However, in the context of an off-nuclear IMBH it is naturally interpreted as evidence for a Bondi/Bondi–Hoyle–Lyttleton-like inflow with $n(r) \propto r^{-3/2}$, since the best-fitting value for the external medium density power-law index, $k = 1.60 \pm 0.17$, is consistent with the value of $k = 3/2$ expected in such a scenario (which we adopt in § 3). The inferred beaming-corrected kinetic energy remains in the range $E_k \sim 10^{50}$–10^{51} erg for reasonable choices of ϵ_e and ϵ_B, which we later compare to the accretion-powered jet budget.

3 INFERRING THE IMBH MASS

3.1 A simple picture: an IMBH at rest in the ISM

Since the source is offset from the centre of its host galaxy by ~ 5.7 kpc, and appears to lie in the galaxy's disc, it is likely surrounded by the interstellar medium (ISM), of number density $n_{\rm ISM} = n_0\,\mathrm{cm}^{-3}$, rest mass density $\rho_{\rm ISM} \approx n_{\rm ISM} m_p$, and sound speed $c_s = c_{s,6} 10^6\,\mathrm{cm\,s}^{-1}$. Here, we make the simple assumption that the IMBH is at rest relative to the ISM, while at § 3.2 we examine alternative scenarios. Under our assumption here, an IMBH would accrete the surrounding ISM in a quasi-spherical Bondi-like flow. Such a flow is established within the Bondi radius,

$$R_{\rm B} = \frac{2GM_\bullet}{c_s^2} = 0.86\, M_{\bullet,4}\, c_{s,6}^{-2}\,\mathrm{pc}\,, \tag{1}$$

where $M_\bullet = M_{\bullet,4} 10^4\,\mathrm{M}_\odot$ in the IMBH mass. Within $r < R_{\rm B}$ matter is accreted radially at close to the local Keplerian velocity, $v \approx v_{\rm K} = \sqrt{GM_\bullet/r} \propto r^{-1/2}$, such that a steady-state constant $\dot{M}_{\rm acc} = 4\pi r^2 \rho(r) v(r)$, implies a density profile $\rho(r) \propto n(r) \propto r^{-3/2}$ (with $k = 3/2$), or $n(r) \approx n_{\rm ISM} \max[1, (r/R_{\rm B})^{-3/2}]$. For a given ISM density $n_{\rm ISM}$, the density normalization within the stratified region ($r < R_{\rm B}$) is determined by the value of the Bondi radius $R_{\rm B}$, which in turn depends on the IMBH mass, $M_\bullet$. Since this density normalization is determined by our fit to the afterglow data, it can therefore be used to infer $M_\bullet$, which is of great interest. In § 2, we have derived $\log_{10}(n_{0,d}) = 0.36 \pm 0.28$, which when requiring $n_{\rm ISM} = n(R_{\rm B})$ implies a Bondi radius of $R_{\rm B} = R_d (n_d/n_{\rm ISM})^{2/3} = R_d (n_{0,d}/n_0)^{2/3} \approx \left(0.56^{+0.31}_{-0.19}\right) n_0^{-2/3}$ pc, and in turn an IMBH mass of

$$M_\bullet \approx \left(6.55^{+3.51}_{-2.29}\right) \times 10^3\, n_0^{-2/3}\, c_{s,6}^2\,\mathrm{M}_\odot\,. \tag{2}$$

This expression makes explicit that our mass estimate is most sensitive to the external density normalization and the sound speed, with $M_\bullet \propto n_0^{-2/3} c_s^2$. A denser or cooler ISM at fixed afterglow normalization implies a lower $M_\bullet$, whereas a more rarefied or hotter ISM pushes $M_\bullet$ upwards. In this sense, the afterglow fit constrains a combination $n_0^{2/3} c_s^{-2} M_\bullet$, and equation (2) is best viewed as a one-parameter family of solutions parametrized by the (not directly measured) ISM properties.

Consistency checks: the value of $M_\bullet$ in equation (2) is consistent with the upper limit from $t_{\rm MV}$ (i.e. $M_\bullet \lesssim 5 \times 10^4\,\mathrm{M}_\odot$) and with the ability to tidally disrupt a white dwarf ($M_\bullet \lesssim 10^5\,\mathrm{M}_\odot$) or main-sequence (MS) star ($M_\bullet \lesssim 10^8\,\mathrm{M}_\odot$). We now show it is self-consistent with:

(i) the assumptions of a Bondi-like accretion flow, and (ii) the afterglow shock propagating in the stratified region ($r < R_B$) during the afterglow observations used in § 2. We emphasize, however, that while this upper-limit argument shows that white-dwarf disruption is in principle possible for the inferred mass scale, the more detailed timing and energetic considerations presented in § 4 disfavour a WD progenitor for GRB 250702B.

(i) The density profile $n(r) \approx n_{\rm ISM} \max[1, (r/R_{\rm B})^{-3/2}]$ implies an enclosed mass of accreting ISM within the Bondi radius,

$$M_B \equiv M(<R_{\rm B}) = \frac{8\pi}{3} R_{\rm B}^3 \rho_{\rm ISM} = 0.132\, n_0\, M_{\bullet,4}^3\, c_{s,6}^{-6}\,\mathrm{M}_\odot\,. \tag{3}$$

This mass rapidly increases with $M_\bullet$, until it equals $M_\bullet$ at a critical mass $M_{\rm cr}$ for which $M_B(M_{\rm cr}) = M_\bullet$, and corresponding radius $R_{\rm cr} = R_B(M_{\rm cr})$, given by

$$M_{\rm cr} = \sqrt{\frac{3c_s^6}{64\pi G^3 \rho_{\rm ISM}}} = 2.75 \times 10^6\, c_{s,6}^3 n_0^{-1/2}\,\mathrm{M}_\odot\,, \tag{4}$$

$$R_{\rm cr} = \sqrt{\frac{3c_s^2}{16\pi G \rho_{\rm ISM}}} = 237\, c_{s,6} n_0^{-1/2}\,\mathrm{pc}\,. \tag{5}$$

We note that up to factors of order unity this corresponds to the Jeans scale ($M_{\rm cr} \sim M_J$, $R_{\rm cr} \sim \lambda_J$). Beyond this scale (i.e. for $M > M_{\rm cr} \sim M_J$), the mass within R_B is dominated by the ISM rather than by $M_\bullet$, and the ISM becomes unstable to gravitational collapse on scales smaller than R_B. Therefore, the assumptions leading to Bondi accretion hold only for $M_\bullet < M_{\rm cr}$. This is indeed consistent with the value of $M_\bullet$ derived in equation (2), and is less constraining than the upper limit from $t_{\rm MV}$.

Fig. 2 shows relevant critical radii versus black hole mass. The narrow vertical shaded grey region shows the inferred 1σ confidence interval on $M_\bullet$ (from equation 2) for $n_0^{-2/3} c_{s,6}^2 = 1$ from our afterglow fit in § 2. The lighter and wider shading indicates a factor of 5 uncertainty in the value of $n_0^{-2/3} c_{s,6}^2$. We note that other works (e.g. J. Carney et al. 2025; B. P. Gompertz et al. 2025) obtain a different external density normalization; while most works fix $k = 2$, the afterglow data typically probes radii of the order of our pivot radius $R_d = 10^{18}$ cm, such that comparison to our $n_d = n(R_d)$ density normalization is meaningful. The inferred values vary by about an order of magnitude in either direction, which

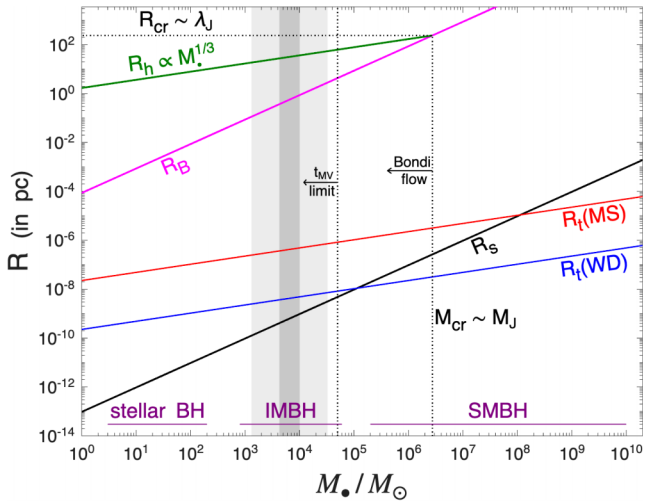

Figure 2. Critical radii R versus black hole mass $M_\bullet$: the tidal radius $R_t = R_*(M_\bullet/M_*)^{1/3}$ for a main sequence (MS) solar-like star ($M_* = \mathrm{M}_\odot$, $R_* = \mathrm{R}_\odot$) and a white dwarf (WD; $M_* = \mathrm{M}_\odot$, $R_* = 0.01\,\mathrm{R}_\odot$), the Schwarzschild radius $R_s = \frac{2GM_\bullet}{c^2}$, the Bondi radius $R_B = \frac{2GM_\bullet}{c_s^2}$ (for $c_{s,6} = 1$), and the radius of influence R_h within which the ISM mass (for $n_0 = c_{s,6} = 1$) equals $M_\bullet$. Two upper limits on $M_\bullet$ are indicated by a vertical dotted line and arrow. The narrow shaded grey region shows the inferred 1σ confidence interval on $M_\bullet$ (from equation 2) for $n_0^{-2/3}\,c_{s,6}^2 = 1$. The lighter and wider shading indicates a factor of 5 uncertainty in the value of $n_0^{-2/3}\,c_{s,6}^2$. Approximate mass ranges are indicated for stellar, intermediate mass (IMBH), and supermassive black holes (SMBH).

corresponds to a factor of ~ 5 in our inferred value of $M_\bullet$, similar to the lighter, wider shading. Finally, a supersonic motion of the IMBH relative to the ISM may lead to an increase in the estimated $M_\bullet$[see § 3.2 and equation (8) below], but it is restricted by the $t_{\rm MV}$ limit, $M_\bullet \lesssim 5\times10^4\,\mathrm{M}_\odot$.

(ii) If the afterglow shock reaches $R_{\rm B}$ a transition will occur to a uniform medium, which would mimic a wind termination shock around a massive star GRB progenitor (e.g. R. A. M. J. Wijers 2001; E. Nakar & J. Granot 2007), without a density jump by a factor of four in the latter case. For an afterglow flux decay $F_\nu \propto t^{-\alpha}$ this would lead to a flattening by $\Delta\alpha = 0.5$ for $\nu_m < \nu < \nu_c$ but would hardly be noticed ($\Delta\alpha \approx 0$) for $\nu > \max(\nu_m, \nu_c)$ (J. Granot & R. Sari 2002; E. Nakar & J. Granot 2007). For an afterglow jet of initial isotropic equivalent energy $E_{\rm k,iso}$ and half-opening angle $\theta_j = 10^{-1.5}\theta_{j,-1.5}$ this will occur before the jet break time t_j if $E_{\rm k,iso} > M_B c^2\theta_j^{-2} + 2.36\times10^{56}\,\theta_{j,-1.5}^{-2} n_0\,M_{\bullet,4}^3\,c_{s,6}^{-6}$ erg. Moreover, for a highly stratified external density profile, the jet break is very gradual (e.g. J. Granot 2007; F. De Colle et al. 2012), and may easily be missed. In our modelling the jet break occurs early, after a few hours, such that most of the afterglow observations are at $t > t_j$. In this case, when neglecting the jet's lateral spreading the $t_{\rm B}$ transition occurs at observed time $t_{\rm B} \approx 78 n_0\,E_{\rm k,iso,54.5}^{-1} M_{\bullet,4}^4\,c_{s,6}^{-8}$ d. If ν_c was well above the *Chandra* energy range (which is at best only marginally valid), then the lack of a flattening in the X-ray light curve up to the second *Chandra* observation (R. A. Eyles-Ferris et al. 2025; R. A. J. Eyles-Ferris et al. 2025), would imply $t_{\rm B} > 65$ d and in turn $M_\bullet \gtrsim 9.5\times10^3 E_{\rm k,iso,54.5}^{1/4} c_{s,6}^2\,\mathrm{M}_\odot$.

For fast lateral spreading the Lorentz factor drops exponentially with radius beyond the jet break radius, R_j, where $R_j/R_B \approx 0.056(E_{\rm k,iso,54.5}/n_0)^{2/3}\,M_{\bullet,4}^{-2}\,c_{s,6}^4$ and the jet becomes non-relativistic at a radius $\sim R_j(1-\ln\theta_j)$. In this case, the jet may become non-relativistic before reaching R_B ($t_{\rm nr} < t_B$), but then the non-relativistic transition will be observed at

$$t_{\rm nr} \approx 100\,\frac{1-\ln\theta_j}{1-\ln 10^{-1.5}} E_{\rm k,51}^{2/3} n_0^{-2/3} M_{\bullet,4}^{-1} c_{s,6}^2\,\mathrm{days}\,, \tag{6}$$

where $E_{\rm k} = 10^{51}E_{\rm k,51}$ erg is the jet's true kinetic energy. Note that the transition at $t_{\rm nr}$ should be apparent also above ν_c, more clearly applying to the X-rays. In this picture, the flux decay rate a $t > t_{\rm nr}$ (but before reaching the deep-Newtonian regime, e.g. J. Granot et al. 2006) is generally given by $F_{\nu>\nu_{m,c}} \propto t^{-\frac{(15-4k)p-20+10k}{10-2k}}$ or $F_{\nu_m<\nu<\nu_c} \propto t^{-\frac{(15-4k)p-21+8k}{10-2k}}$. For $k=\frac{3}{2}$ at $t<t_B$ this implies $F_{\nu>\nu_{m,c}}(t_{\rm nr}<t<t_B) \propto t^{-\frac{9p-5}{7}}$ ($1.99\le\alpha\le2.11$ for $2.1\le p\le 2.2$) or $F_{\nu_m<\nu<\nu_c}(t_{\rm nr}<t<t_B) \propto t^{-\frac{9(p-1)}{7}}$ ($1.41\le\alpha\le1.54$ for $2.1\le p\le2.2$) which at $t > t_B$ transitions to $k=0$ which implies $F_{\nu>\nu_{m,c}}(t_{\rm nr}<t_B<t) \propto t^{-\frac{3p-4}{2}}$ ($1.15\le\alpha\le1.3$ for $2.1\le p\le2.2$) or $F_{\nu_m<\nu<\nu_c}(t_{\rm nr}<t_B<t) \propto t^{-\frac{15p-21}{10}}$ ($1.05\le\alpha\le1.2$ for $2.1\le p\le2.2$). If $t_{\rm nr} \sim t_B$ then the flux decay would directly transition at this time to the latter slopes.

3.2 Other scenarios for an IMBH in the host galaxy

Here, we consider alternative scenarios for an IMBH within its host galaxy, such as: (i) having a significant speed $v_{\rm BH} \gtrsim c_s$ relative to the local ISM, (ii) being located at the centre of a star cluster, or (iii) becoming episodically embedded in a gas-rich region that assembles a long-lived 'mini-AGN' (mAGN) disc (M. Rozner et al. 2025).

(i) Fast moving IMBH: in scenario (i), the Bondi accretion flow is replaced by a Bondi–Hoyle–Lyttleton (BHL) accretion flow. The simplest version of the latter is steady in the BH's frame and axisymmetric about the direction of $v_{\rm BH}$. It is convenient to parameterize this flow using the BH's Mach number relative to the ISM, $\mathcal{M} \equiv v_{\rm BH}/c_s$. In the BH's frame, in the supersonic case ($\mathcal{M} > 1$), simulations show (e.g. M. Livio et al. 1986; J. M. Blondin & E. Raymer 2012; W. Xu & J. M. Stone 2019) that a bow shock forms ahead of the central mass (BH), where the matter that remains bound accretes onto it in a flow that resembles a Bondi flow at $r < R_{\rm BHL}$ where[1]

$$R_{\rm BHL} \approx \frac{R_B}{1+\mathcal{M}^2} = \frac{2GM_\bullet}{c_s^2(1+\mathcal{M}^2)} = 0.86\,\frac{M_{\bullet,4}\,c_{s,6}^{-2}}{1+\mathcal{M}^2}\,\mathrm{pc}\,, \tag{7}$$

where $R_{\rm BHL}$ is the Bondi–Hoyle–Lyttleton radius, which generalizes the Bondi radius. Up to factors of order unity, the density profile could be approximated by $n(r) \approx n_{\rm ISM}\max[1, (r/R_{\rm BHL})^{-3/2}]$, and our derived BH mass is generalized to

$$M_\bullet \approx \left(6.55^{+3.51}_{-2.29}\right)\times10^3\,n_0^{-2/3}\,c_{s,6}^2(1+\mathcal{M}^2)\,\mathrm{M}_\odot\,, \tag{8}$$

i.e. it increases by a factor of $1+\mathcal{M}^2$ (or $\sim\mathcal{M}^2$ for $\mathcal{M} > 1$) relative to pure Bondi accretion ($\mathcal{M} = 0$). Because $M_\bullet \propto n_0^{-2/3}c_s^2(1+\mathcal{M}^2)$ (equation 8), higher upstream density and lower sound speed both act to *reduce* the inferred $M_\bullet$ at fixed afterglow normalization, while larger IMBH–gas Mach number increases it through the $(1+\mathcal{M}^2)$ factor.

[1]Note that $R_{\rm BHL}$ is of the order of the downstream Bondi radius $R_{B,d}$. For weak shocks ($\mathcal{M}\sim1$) both $R_{\rm BHL}\sim R_B\sim R_{B,d}$, where $R_{B,d} \sim R_B$ since the downstream and upstream sound speeds are comparable, $c_{s,d} \sim c_s$. For a strong shock it follows the scaling $R_B \propto c_s^{-2} \sim \frac{\rho}{p}$ where the pressure increases by a factor of $\sim\mathcal{M}^2$ while the density increases by a factor of 4.

Using our upper limit on $M_\bullet$ from the source-frame rapid variability time $t_{\rm MV,src} = \frac{t_{\rm MV}}{1+z} \approx 0.5\,{\rm s}$ of GRB 250702B, $M_\bullet \lesssim 5 \times 10^4\,{\rm M}_\odot$, we obtain an upper limit on $\mathcal{M}$ and on $v_{\rm BH}$,

$$\mathcal{M} \equiv \frac{v_{\rm BH}}{c_s} \lesssim 2.8\, n_0^{1/3} c_{s,6}^{-1} \implies v_{\rm BH} \lesssim 28\, n_0^{1/3}\,{\rm km\,s^{-1}}\,. \quad (9)$$

This upper limit is barely consistent with the escape velocity from the centre of a globular cluster ($v_{\rm esc} \sim 30{-}100\,{\rm km\,s^{-1}}$), where an IMBH may be naturally formed (J. E. Greene, J. Strader & L. C. Ho 2020). None the less, such an escaping IMBH with $v_{\rm BH} \sim v_{\rm esc} \lesssim 30\,{\rm km\,s^{-1}}$ might still be consistent with the observations for GRB 250702B. Even for an escape at a slightly higher velocity, the IMBH's velocity relative to the ISM $v_{\rm BH}$ may be damped over time because of dynamical friction with gas or stars.

(ii) IMBH at the center of a star cluster: if the IMBH resides in a star cluster, the ambient gas is set by the competition between stellar mass loss (e.g. asymptotic giant branch – AGB winds) and clearing by pulsar/ultraviolet (UV) feedback and/or ram pressure as the cluster moves through the host ISM. In old Milky Way globulars the steady-state gas content is generally very low, with typical central densities $n_{\rm gas} \sim 10^{-3}$–$10^{-1}\,{\rm cm^{-3}}$ and stringent upper limits in several systems (P. C. Freire et al. 2001; I. McDonald & A. A. Zijlstra 2015); episodic retention (e.g. in core-collapsed/massive clusters) can temporarily raise $n_{\rm gas}$ to $\sim$0.1–1 $\rm cm^{-3}$ before feedback re-clears the core (e.g. see A. Bobrick, M. B. Davies & H. B. Perets 2025, and references therein). Higher, more sustained gas levels are plausible in young massive or nuclear clusters. The IMBH speed relative to the local gas is at most comparable to the cluster one-dimensional stellar velocity dispersion, $\sigma_\star \sim 5$–$20\,{\rm km\,s^{-1}}$ for old globulars and up to a few $10\,{\rm km\,s^{-1}}$ in compact massive systems, implying $v_{\rm BH} \sim \sigma_\star$. For warm gas ($T \sim 10^4\,{\rm K}$; $c_s \sim 8$–$12\,{\rm km\,s^{-1}}$), this gives $\mathcal{M} \equiv v_{\rm BH}/c_s \sim 0.5$–2 (and larger $\mathcal{M}$ in colder gas). In this regime the flow is well described by Bondi–Hoyle–Lyttleton accretion, for which we have derived an upper limit on $v_{\rm BH}$ in equation (9), $v_{\rm BH} \lesssim 28\, n_0^{1/3}\,{\rm km\,s^{-1}}$, so a cluster-core IMBH with $\sigma_\star \sim 10$–$25\,{\rm km\,s^{-1}}$ is consistent with our constraints provided the gas is warm (or $n_0 \gtrsim 1$). Episodes of enhanced gas retention (or passages through denser clumps) would increase the normalization of $n(r)$ and, at fixed k, reduce the $M_\bullet$ required by the afterglow fit, while gas-poor phases do the opposite. For $n_{\rm gas} \sim 0.1$–$10\,{\rm cm^{-3}}$ and $c_s \sim 5$–$15\,{\rm km\,s^{-1}}$, the Bondi radius (given in equation 1), is $\sim$ 0.1–1 pc, large enough that the blast wave remains within the $n \propto r^{-3/2}$ zone over the epochs used in our fit, consistent with the measured $k = 1.60 \pm 0.17$.

(iii) IMBH embedded in a gas-rich mini-AGN disc: an IMBH traversing or residing in a gas-rich clump can assemble a rotationally supported 'mini-AGN' (mAGN) disc that sustains an elevated ambient density and mass-supply rate (M. Rozner et al. 2025). In the Bondi/BHL language, this raises the effective upstream density and can modify the sound speed. The relevant gravitational 'capture radius' that sets the inner $n \propto r^{-3/2}$ region is the Bondi–Hoyle–Lyttleton scale $R_{\rm BHL}$ (equation 7), which reduces to the Bondi radius R_B for $\mathcal{M} = 0$. Inside $r \lesssim R_{\rm BHL}$ the steady inflow approaches $n(r) \propto r^{-3/2}$, so the afterglow normalization implies (cf. equation 8),

$$M_\bullet \;\propto\; n_0^{-2/3}\, c_s^2\, \left(1 + \mathcal{M}^2\right).$$

Sign of the effect: increasing the mid-plane density (larger n_0) or lowering the sound speed (smaller c_s) in an mAGN generally *decreases* the $M_\bullet$ inferred from the same afterglow fit, whereas a larger relative shear (higher $\mathcal{M}$) *increases* it through the $(1 + \mathcal{M}^2)$ factor. Thus, a cool, dense mAGN mid-plane tends to lower the inferred $M_\bullet$ unless the IMBH–gas motion is sufficiently supersonic to compensate.

4 A MILLI-TDE MAIN-SEQUENCE STAR MODEL FOR GRB 250702B

Here, we discuss how an mTDE scenario can explain the different observational properties of GRB 250702B or possibly of ultralong GRBs (ULGRBs) in general. The classical GRB duration distribution is bimodal, consisting of short ($\sim 10^{-2.5}$–$10^{0.5}$ s) and long ($\sim 10^{0}$–$10^{2.5}$ s) GRBs, arising respectively from compact binary mergers and the collapse of massive stars (D. Eichler et al. 1989; C. Kouveliotou et al. 1993; S. E. Woosley 1993). ULGRBs of durations $\gtrsim 10^3$ s (e.g. B. Gendre et al. 2013; A. J. Levan et al. 2014; M. Boër et al. 2015; J. Greiner et al. 2015; B. Gendre 2025) form a small separate population, and appear to be distinct not only in the GRB duration distribution but also in their prompt emission spectral properties and host galaxy types (diverse prompt emission, spectral shapes, and host demographics) suggesting that ULGRBs may comprise multiple physical channels rather than a single progenitor class (B. Gendre et al. 2013; A. J. Levan et al. 2014; J. Greiner et al. 2015).

Their diverse prompt emission light-curve shapes and spectra, along with mixed evidence on possible accompanying supernovae, may even suggest that ULGRBs may comprise multiple physical channels and/or sub-classes rather than a single progenitor class (B. Gendre et al. 2013; A. J. Levan et al. 2014; J. Greiner et al. 2015). GRB 250702B extends this population to an extreme regime (E. Neights et al. 2025a) in both duration ($T_{90} \approx 2.5 \times 10^4$ s) and energetics ($E_{\gamma,\rm iso} \gtrsim 1.4 \times 10^{54}$ erg), while also exhibiting a day-scale, gradually rising soft X-ray emission episode (with $E_{\rm X,iso} \gtrsim 10^{52}$ erg; D. Y. Li et al. 2025). Any viable model must therefore explain not only the ultralong duration, but also the structured temporal behaviour across $\sim$ five decades in time, from sub-second variability to $\sim 10^5$ s.

So far, we have shown that an mTDE model can, in principle, explain the observed short time-scale variability of GRB 250702B, as well as its external density profile and normalization, which provide a self-consistent estimate of $M_\bullet$. The main remaining observations that an mTDE model needs to explain are the duration (> 12 ks, where all quantities here are in the source's cosmological frame) and energetics of the main gamma-ray emission episode ($E_{\gamma,\rm iso} \gtrsim 1.4 \times 10^{54}$ erg), as well as the pre-peak gradually rising emission ($E_{\rm X,iso} \gtrsim 10^{52}$ erg) X-ray emission, which started about half a day earlier.

4.1 Emission time-scales and energetics

A star of mass $M_* = M_{*,0}\,{\rm M}_\odot$ and radius $R_* = R_{*,0}\,{\rm R}_\odot$ is tidally disrupted near the tidal radius $r_{\rm t} \equiv R_*(M_\bullet/M_*)^{1/3}$, or more precisely at $\eta^{2/3} r_{\rm t}$, where we introduce a dimensionless factor η to encapsulate order-unity corrections to the simple Roche limit estimate (due to internal stellar structure, spin, etc.). The canonical tidal radius expression $r_{\rm t} = R_*(M_\bullet/M_*)^{1/3}$ is known to carry an order-unity prefactor that is sensitive to hydrodynamic and self-gravitational effects and is best calibrated numerically (e.g. E. M. Rossi et al. 2021), while detailed disruption calculations with realistic stellar models show that internal structure mainly affects the energy and fallback distribution rather than introducing large multiplicative changes to $t_{\rm t}$ (e.g. G. Lodato, A. R. King & J. E. Pringle 2009; J. Guillochon & E. Ramirez-Ruiz 2013; N. Stone,

R. Sari & A. Loeb 2013). The depth of penetration relative to the tidal radius determines the disruption strength and is usually parameterized by the penetration factor, $\beta \equiv r_t/r_p$, where r_p is the peri-centre distance. Deep encounters with $\beta \gtrsim 1$ typically yield complete disruptions (in which about half of the star's mass becomes bound while the other half escapes, for an initial parabolic orbit), while shallower encounters ($\beta \lesssim 1$) can lead to partial disruptions and repeated stripping events (e.g. E. R. Coughlin & C. J. Nixon 2019; Y.-H. Wang, R. Perna & P. J. Armitage 2021; P. Vynatheya et al. 2024; C. Xin et al. 2024).

We consider an MS sun-like star with $M_{*,0} \sim R_{*,0} \sim 1$ and a white dwarf (WD) with $M_{*,0} \sim 1$ and $R_{*,-2} = R_*/(0.01\,\mathrm{R}_\odot) \sim 1$. The time from the stellar disruption at r_t to the first periastron passage at r_p depends only on the properties of the disrupted star (and not on $M_\bullet$) and is approximately given by

$$t_1 = \sqrt{\frac{\pi^2 R_*^3}{2GM_*}} = \begin{cases} 3.54\times10^3 R_{*,0}^{3/2} M_{*,0}^{-1/2}\,\mathrm{s} & (\mathrm{MS})\,, \\ 3.54\, R_{*,-2}^{3/2} M_{*,0}^{-1/2}\,\mathrm{s} & (\mathrm{WD})\,. \end{cases} \tag{10}$$

The most bound material acquires a semimajor axis $a_{\rm min} \approx \eta^{4/3} A_\beta^{2/3} r_t^2/2R_*$ and an orbital time

$$t_{\rm min} \approx \begin{cases} 3.5\times10^4\, A_{\beta,-1}\,\eta^2\, M_{\bullet,4}^{1/2}\, R_{*,0}^{3/2}\, M_{*,0}^{-1}\,\mathrm{s} & (\mathrm{MS})\,, \\ 3.5\times10^1\, A_{\beta,-1}\,\eta^2\, M_{\bullet,4}^{1/2}\, R_{*,-2}^{3/2}\, M_{*,0}^{-1}\,\mathrm{s} & (\mathrm{WD})\,. \end{cases} \tag{11}$$

where the parameter $A_\beta = 10^{-1} A_{\beta,-1}$ (P. Beniamini et al. 2025) depends on the star's response to the tidal field, ranging from 1 for the 'frozen in' approximation to $\sim \beta^{-3}$ if energy is efficiently dissipated near r_p, which we consider to be more realistic (e.g. J. Guillochon & E. Ramirez-Ruiz 2013; N. Stone et al. 2013; E. R. Coughlin & C. Nixon 2015). For a deep encounter with $\beta \sim 3$ and $A_\beta \sim \beta^{-3}$ we have $t_{\rm min} \sim 3.6$ h for an MS star, while a WD may not form an accretion disc at all and instead directly plunge in since $r_p \sim 3.4 r_g$ may be smaller than $r_{\rm ISCO}$ (the radius of the innermost stable circular orbit – ISCO). Since the most bound material falls back first, $t_{\rm min}$ sets the onset time of accretion.

We can see that for a WD (even with a marginal $\beta \approx 1$), the characteristic time-scales are far too short compared to GRB 250702B (see also B. O'Connor et al. 2025). A more detailed analysis, making explicit use of the observed intra-episode spacing $\Delta t_{\rm ep} \approx 2.8\times10^3$ s, the total prompt duration, and the energetics, shows that WD–IMBH encounters are in strong tension with the data even before invoking detonation limits. Interpreting $\Delta t_{\rm ep}$ as an orbital or fallback-based clock selects $t_{\rm min} \sim 20$–60 s, which is natural for low-mass WDs but then implies engine lifetimes that are much shorter than the observed multihour prompt phase. Conversely, choosing $t_{\rm min}$ large enough to power a hours-long engine is incompatible with the recurrence time-scale. Together with the limited mass that can be stripped in non-detonating passages, this effectively rules out a WD–IMBH origin for GRB 250702B, and from this point onwards, we therefore focus on a main-sequence progenitor in the mTDE framework, defined as MS–mTDE.

GR precession, self-intersection, circularization: at $r_p = r_t/\beta$ the general-relativistic (GR) apsidal precession per orbit is

$$\Delta\varpi = \frac{6\pi r_g}{(1+e)r_p} \approx 3\pi\,\frac{r_g}{r_p} \approx 0.93\times10^{-2}\,\beta\,\frac{M_{\bullet,4}^{2/3} M_{*,0}^{1/3}}{R_{*,0}}\,, \tag{12}$$

for a highly eccentric orbit ($e \approx 1$). Efficient prompt circularization requires significant stream self-intersection (with a large relative velocity of the two streams at the intersection point, comparable to the local Keplerian velocity), which in turn requires precession exceeding the stream thickness, $\Delta\varpi \gtrsim H/R$, with debris-stream $H/R \sim 10^{-2}$–10^{-1}. Because $\Delta\varpi$ is small for MS–mTDE encounters, prompt intersection is uncertain unless aided by pressure or Lense–Thirring precession. None the less, each successive periastron pass leads to additional dissipation, which tends to decrease the semimajor axis a and corresponding orbital time $P \propto a^{3/2}$, such that successive passages tend to take less time. If $P_i = q^{i-1} t_{\rm min}$ with some $q < 1$ the cumulative time for m passages is $t_m = \sum_{i=1}^m P_i = \frac{1-q^{m-1}}{1-q} t_{\rm min} < \frac{t_{\rm min}}{1-q}$. Hence, we adopt a conservative circularization multiplier

$$f_{\rm circ} \equiv \frac{t_{\rm circ}}{t_{\rm min}} \sim \mathcal{O}(1\text{-}10)\,, \tag{13}$$

with lower values favoured when precession or thickness aid intersection. Recent analytic and simulation work shows that stream self-intersection and stream–disc shocks can power early emission and that circularization may be delayed for weak precession typical of IMBH–MS encounters (K. Hayasaki, N. Stone & A. Loeb 2016; W. Lu & C. Bonnerot 2020; J. Rossi, J. Servin & M. Kesden 2021; E. Steinberg & N. C. Stone 2024). For μTDEs by stellar-mass BHs, simulations likewise find that circularization efficiency depends sensitively on β and flow thickness (K. Kremer et al. 2023; P. Vynatheya et al. 2024), and $f_{\rm circ}$ of order a few is plausible when vertical thickness or nodal precession aid intersections.

The different time-scales: the circularization and viscous time-scales of the debris disc also affect the effective accretion time. The local viscous time is $t_{\rm vis} \approx [\alpha h^2 \Omega_{\rm K}(r)]^{-1}$ where $\Omega_{\rm K} = v_{\rm K}/r = (GM/r^3)^{1/2}$ is the local Keplerian angular velocity, $\alpha = 10^{-1}\alpha_{-1}$ is the disc viscosity parameter and $h = H/R$ is the disc aspect ratio. If the infalling material circularizes near twice the peri-centre distance (consistent with most of the dissipation occurring near r_p), then $R_{\rm circ} \simeq 2r_p = 2r_t/\beta$. This leads to an accretion (i.e. viscous inflow) time-scale of $t_{\rm acc} \approx t_{\rm vis}(R_{\rm circ})$, i.e.

$$t_{\rm acc} \approx 4.5\times10^4\,\beta^{-3/2}\,\alpha_{-1}^{-1}\,h^{-2}\,M_{*,0}^{-\frac{1}{2}}\,R_{*,0}^{3/2}\,\mathrm{s}\,. \tag{14}$$

The large isotropic equivalent energy of the pre-peak X-ray emission, $E_{\rm X,iso} \gtrsim 10^{52}$ erg, suggests that it is beamed and arises from the relativistic jet (on energetic grounds – see discussion at the end of this section). Its gradual rise towards the peak also supports a common origin with the main emission, which must arise much more clearly from a relativistic jet. It appears most likely that the pre-peak emission corresponds to the early stages of the circularization of the fallback accretion stream and the formation of an accretion disc, as this may naturally produce the gradual rise towards the peak. Therefore, its duration is expected to be of the order of $t_{\rm X,rise} \sim t_{\rm circ} + t_{\rm acc}$. As the accretion rate $\dot{M}_{\rm acc}$ gradually increases, it can support a larger magnetic flux near the IMBH, which can lead to a larger jet power. Moreover, the initial circularization likely leads to a larger baryon loading in the jet and a lower Lorentz factor. As circularization is completed and the magnetic field anchored in the accretion disc near the BH reaches equipartition values it may inhibit significant baryon loading into the jet, allowing for a larger Lorentz factor during the main emission episode, and correspondingly stronger beaming of the emitted radiation (and a narrower jet with a smaller beaming factor $f_b \simeq \frac{1}{2}\theta_j^2$).

In such a scenario, we expect the duration of the main emission episode, $t_{\rm main}$, to correspond to the time over which $\dot{M}_{\rm acc}$ is near its peak value, roughly of the order of $t_{\rm min} + t_{\rm acc} = f_{\rm circ}^{-1} t_{\rm circ} + t_{\rm acc}$.

Adopting here $A_\beta \approx \beta^{-3}$ and $\beta_{0.5} = \beta/10^{0.5}$ leads to

$$\begin{aligned} &t_{\rm X,rise} \sim t_{\rm circ} + t_{\rm acc}\,, \qquad t_{\rm main} \sim t_{\rm min} + t_{\rm acc}\,,\\ &t_{\rm circ} \approx 3.5\times10^4 f_{0.5}\beta_{0.5}^{-3}\,\eta^2\,M_{\bullet,4}^{1/2}\,R_{*,0}^{3/2}\,M_{*,0}^{-1}\,{\rm s}\,,\\ &t_{\rm min} \approx 1.1\times10^4 \beta_{0.5}^{-3}\,\eta^2\,M_{\bullet,4}^{1/2}\,R_{*,0}^{3/2}\,M_{*,0}^{-1}\,{\rm s}\,,\\ &t_{\rm acc} \approx\ 3.2\times10^4\,\beta_{0.5}^{-3/2}\,\alpha_{-1}^{-1}\,h_{-0.3}^{-2}\,M_{*,0}^{-\frac{1}{2}}\,R_{*,0}^{3/2}\,{\rm s}\,, \end{aligned} \tag{15}$$

where $f_{0.5} = f_{\rm circ}/10^{0.5}$, $h_{-0.3} = h/10^{-0.3} \approx 2h$. For an MS star the mass–radius relation follows $R_* \propto M_*^s$ with $s \approx 0.8$ such that $t_{\rm circ} \propto R_*^{3/2}M_*^{-1} \propto M_*^{(3s-2)/2} \approx M_*^{0.2}$ only weakly depends on M_*, while $t_{\rm acc} \propto M_*^{-1/2}R_*^{3/2} \propto M_*^{(3s-1)/2} \approx M_*^{0.7}$ has a somewhat stronger dependence.

For a concrete fiducial example, taking a solar-type star ($M_{*,0} = R_{*,0} = 1$), an IMBH mass $M_{\bullet,4} \sim 0.7$ as suggested by equation (2), a moderately deep encounter $\beta \sim 3$ ($\beta_{0.5} \approx 0.95$), $\alpha_{-1} \sim 1$ and $h_{-0.3} \sim 1$, we obtain $t_{\rm min} \sim 10^4$ s, $t_{\rm acc} \sim$ few $\times\, 10^4$ s and $t_{\rm circ} \sim$ few $\times\, 10^4$ s for $f_{\rm circ} \sim$ few. These values are naturally of the same order as the observed source-frame durations of the pre-peak X-ray rise and main prompt phase, showing that the mTDE time-scales for an MS star around a $\sim 10^4\,{\rm M}_\odot$ IMBH are in the right ballpark without fine-tuning.

The fast rise to the main peak may be due to an instability in the accretion disc, which either boosted the jet power or increased its Lorentz factor and collimation, possibly by reducing the baryon loading as strong large-scale magnetic fields are established near the IMBH.

The bright emission episodes (e.g. four *Fermi*–GBM triggers; E. Neights et al. 2025a) within the main part of the emission may reflect cycles near the inner flow (e.g. through a magnetically arrested disc – MAD flux gating or interchange, or radiation–pressure thermal cycles), then a natural time-scale is the local viscous (or thermal) time $t_{\rm vis} = t_{\rm acc}(r/R_{\rm circ})^{3/2}$,

$$t_{\rm vis} \approx \frac{r^{3/2}}{\sqrt{GM_\bullet}\,\alpha h^2} = 1.24\times10^3\,r_2^{3/2}M_{\bullet,3.8}^{-1/2}\alpha_{-1}^{-1}\,h_{-0.3}^{-2}\,{\rm s}\,, \tag{16}$$

where $r_2 = r/(100\,r_g)$. Typical source frame emission episode durations of ~ 1–2 ks would correspond to radii $r \sim (85$–$140)r_g$.

Thus, if the bright episodes reflect quasi-cyclic behaviour in the inner flow (e.g. magnetically arrested disc flux accumulation and interchange, or radiation–pressure-driven thermal–viscous cycles), the observed $\sim 10^3$ s spacing can be interpreted as the local viscous/thermal time at $r \sim 10^2\,r_g$. This interpretation is attractive because it ties the episode spacing directly to accretion physics rather than to an orbital clock at $r \gg r_t$, and it automatically scales with $M_\bullet$ in the same way as $t_{\rm acc}$.

Main emission energetics: as for the energetics of the main emission episode, our afterglow modelling requires a total true (beaming-corrected) kinetic energy in a narrow relativistic jet of $E_k \lesssim 10^{51}$ erg. For an accreted mass of $\sim 0.5\,{\rm M}_\odot$ this corresponds to a reasonable jet launching efficiency of $\eta_j \sim 10^{-3}$. An alternative parametrization following P. Beniamini et al. (2025) requires an accreted mass of $M_{\rm acc} \approx 0.35\,\eta_{\gamma,-1}^{-1}\,\theta_{\rm j,-1.5}^2\,\eta_{\rm j,-2}^{-1}\,{\rm M}_\odot$ where $\eta_\gamma = 10^{-1}\eta_{\gamma,-1} = E_{\rm k,iso}/E_{\gamma,\rm iso}$, $\theta_j = 10^{-1.5}\theta_{j,-1.5}$ is the jet half-opening angle and $\eta_j = 10^{-2}\eta_{j,-2} = L_j/\dot{M}_{\rm acc}c^2$ is the jet launching efficiency. Here, $\eta_j \sim 10^{-2}$ and $\eta_\gamma \sim 0.1$ are assumed. In the context of active galactic nucleus (AGN), general-relativistic magnetohydrodynamical (GRMHD) simulations show that jet efficiencies span $\eta_j \sim 10^{-3}$–10^{-1} depending on BH spin, magnetic flux, and whether the flow attains a magnetically arrested (MAD) state; values $\gtrsim 10$ per cent are obtained for high spin in MAD discs (A. Tchekhovskoy, R. Narayan & J. C. McKinney 2011; J. C. McKinney, A. Tchekhovskoy & R. D. Blandford 2012). Such simulations assume a constant black hole spin, and are therefore not directly applicable to stellar-mass black holes where the accretion and jet launching can significantly change the BH spin if the accreted mass is comparable to $M_\bullet$, [e.g. Z.-F. Wu et al. 2025 found that magnetically (Blandford–Znajek) powered jets in GRBs have a maximal efficiency of $\eta_{\rm j} \sim 0.015$]. While the beaming factor of $f_b \approx \frac{1}{2}\theta_j^2 \sim 0.5 \times 10^{-3}$ used above ($\theta_{j,-1.5}$) is ~ 10 times larger than the best-fitting value from our afterglow fit, it is still compatible with it (see also equation 18 below). Our best-fitting value of $f_b \sim 10^{-4}$ leads to a similar required accreted mass for $\eta_\gamma \sim 0.1$ and $\eta_j \sim 10^{-3}$. Since the accreted mass in a TDE is much smaller than that of an IMBH, in our scenario the IMBH's dimensionless spin a plays an important role in determining the jet launching efficiency, which for relatively small values of a is limited to $\eta_{\rm BZ} \lesssim 0.25a^2$ (e.g. A. Tchekhovskoy, J. C. McKinney & R. Narayan 2012). This will in turn require a minimal spin parameter of $a \gtrsim 0.06\eta_{j,-3}^{1/2}$. Altogether, the energy requirements are reasonably met in an mTDE MS star scenario. Moreover, the beaming-corrected kinetic energy inferred from the afterglow modelling, $E_k \lesssim 10^{51}$ erg, is comfortably below the maximum budget available from accreting ~ 0.3–$0.5\,{\rm M}_\odot$ with $\eta_j \sim 10^{-3}$–10^{-2} and $\eta_\gamma \sim 0.1$. In other words, the same parameter choices that reproduce the prompt γ-ray energetics are fully compatible with the independently inferred afterglow energetics, reinforcing the internal consistency of the mTDE interpretation.

Explicit beaming–efficiency constraint: One can reverse the argument in order to derive a limit on the beaming that is independent of the afterglow modelling. The beaming-corrected prompt energy requires

$$M_{\rm acc} = \frac{f_b\,E_{\gamma,\rm iso}}{\eta_\gamma\,\eta_j\,c^2}. \tag{17}$$

Requiring $M_{\rm acc} \le M_{\rm fb} = f_{\rm fb}M_*$, where $M_{\rm fb}$ and $f_{\rm fb}$ are the fallback mass and fraction, respectively, implies

$$f_b \le 6.4\times10^{-4}\eta_{j,-2}\eta_{\gamma,-1}M_{*,0}\left(\frac{f_{\rm fb}}{0.5}\right)\left(\frac{1.4\times10^{54}\,{\rm erg}}{E_{\gamma,\rm iso}}\right), \tag{18}$$

or correspondingly, $\theta_j \approx (2f_b)^{1/2} \lesssim 0.036$ rad.

4.2 Expected event rates versus inferred ultralong GRB rates

Ultralong GRBs (ULGRBs; $T_{90} \gtrsim 10^3$ s) are rare in *Swift* burst alert telescope (BAT) samples. A systematic search in the third BAT catalogue finds 15 ULGRBs, $\simeq 2$ per cent of BAT GRBs, with confirmed emission beyond $\sim 10^3$ s (A. Lien et al. 2016). Other compilations and case studies (e.g. A. J. Levan et al. 2014; S. Wet et al. 2023) similarly indicate a per cent-level occurrence among prompt-detected events. There is also evidence that selection effects (in particular, the difficulty of detecting long, relatively faint emission tails) bias against ULGRBs, so this fraction should be regarded as a lower limit on the true underlying incidence (e.g. A. J. Levan et al. 2014).

Using the local *observed* long-GRB (LGRB) rate density $R_{\rm LGRB,obs} \sim 1$–$2\ {\rm Gpc^{-3}\,yr^{-1}}$ (e.g. D. Wanderman & T. Piran 2010; G.-X. Lan et al. 2019), a naive observed ULGRB rate is

$$R_{\rm ULGRB,obs} \ \sim\ (2-4)\times10^{-2}\ {\rm Gpc^{-3}\,yr^{-1}}\,, \tag{19}$$

simply scaling with the ~ 2 per cent ULGRB fraction. Correcting for beaming increases the intrinsic rate by $f_b^{-1} = 2/\theta_j^2$. For

a fiducial jet half-opening angle of $\theta_j \sim 2^\circ$–6° (corresponding to $f_b \simeq \frac{1}{2}\theta_j^2 \sim 6\times10^{-4}$–$5\times10^{-3}$) the implied intrinsic rate is

$$R_{\rm ULGRB,int} \sim 1-20\ {\rm Gpc^{-3}\,yr^{-1}}, \quad (20)$$

where the numerical range primarily reflects the uncertainty in the typical ULGRB beaming angle, on top of the small-number statistics of the current sample and possible redshift evolution. This bracket should therefore be regarded as an order-of-magnitude estimate.

These rate estimates can now be compared with mTDE expectations. Dynamical models of star clusters and off-nuclear systems that retain an IMBH generally predict main-sequence tidal-disruption rates per IMBH host of order $\Gamma_{\rm mTDE} \sim 10^{-7}$–$10^{-5}\,{\rm yr^{-1}}$, with a strong dependence on the cluster structure, mass, and IMBH occupation fraction (e.g. N. C. Stone & B. D. Metzger 2016; G. Fragione et al. 2018). Converting to a volumetric rate requires the space density $n_{\rm host}$ of suitable IMBH-bearing systems (massive star clusters, compact dwarfs, off-nuclear nuclei). Adopting a fiducial range[2] $n_{\rm host} \sim 10^6$–$10^8\ {\rm Gpc^{-3}}$ gives

$$R_{\rm mTDE} \simeq \Gamma_{\rm mTDE}\, n_{\rm host} \sim 10^{-1}-10^3\ {\rm Gpc^{-3}\,yr^{-1}}, \quad (21)$$

which largely overlaps with the broad range of $\sim 10^{-2}-10^2\ {\rm Gpc^{-3}\,yr^{-1}}$ spanned by published calculations for different IMBH environments. We stress that $R_{\rm mTDE}$ is uncertain at the order-of-magnitude level, primarily because the census of IMBH-hosting systems is still poorly constrained.

Let $\xi \le 1$ denote the fraction of ULGRBs that are in fact IMBH mTDEs, and let $f_{\rm j}$ be the fraction of mTDEs that successfully launch relativistic jets, which would appear as ULGRBs if pointed close enough to our line of sight (the probability for which is f_b). Matching the intrinsic ULGRB rate to the mTDE pool gives a simple book-keeping relation,

$$f_{\rm j} \simeq \xi\, \frac{R_{\rm ULGRB,int}}{R_{\rm mTDE}}. \quad (22)$$

Here, $R_{\rm ULGRB,int} = f_b^{-1} R_{\rm ULGRB,obs}$ already includes an assumed beaming correction through the choice of $\theta_{\rm j}$; for a different fiducial opening angle both $R_{\rm ULGRB,int}$ and the inferred $f_{\rm j}$ would rescale proportionally.

Using $R_{\rm ULGRB,int} \sim 1$–$20\ {\rm Gpc^{-3}\,yr^{-1}}$ and $R_{\rm mTDE} \sim 0.1$–$10\ {\rm Gpc^{-3}\,yr^{-1}}$ yields a broad allowed range,

$$10^{-1}\,\xi \lesssim f_{\rm j} \lesssim 1. \quad (23)$$

If the true volumetric mTDE rate turns out to be at the high end of current theoretical expectations, $R_{\rm mTDE} \sim 10^2 - 10^3\ {\rm Gpc^{-3}\,yr^{-1}}$, then proportionally smaller jetting fractions $f_{\rm j} \sim 10^{-3}$–10^{-2} with $\xi \sim 1$ would also be consistent. Thus, values $f_{\rm j} \sim 0.03$–0.3 are not strictly required; they are merely favoured if one simultaneously adopts the upper end of $R_{\rm ULGRB,int}$ and the lower end of $R_{\rm mTDE}$ with $\xi \simeq 1$.

In summary, within plausible (but currently broad) assumptions about beaming, jet production efficiency, and IMBH demographics, an mTDE of a MS star by an IMBH can accommodate the observed rarity of ULGRBs while also providing an intrinsic rate comparable to that inferred after beaming corrections. Improved constraints will come from (i) systematic ULGRB searches in survey data (e.g. BAT survey mode) (A. Lien et al. 2016), (ii) host-environment demographics of ULGRBs versus TDEs, and (iii) direct IMBH census work in clusters and dwarf galaxies.

[2]Corresponding roughly to $\sim 10^2$–10^3 potential IMBH hosts per $L_\star$ galaxy, with a sub-unity occupation fraction.

5 DISCUSSION AND SUMMARY

5.1 Summary of the main results

We have explored the hypothesis that GRB 250702B is powered by a milli-tidal disruption event (mTDE) in which an MS star is disrupted by an IMBH. Our multiwavelength afterglow modelling favours a stratified external density profile with $k = 1.60 \pm 0.17$, consistent with quasi-spherical Bondi/Bondi–Hoyle–Lyttleton (BHL) inflow where $n(r) \propto r^{-3/2}$ inside the capture radius. Using the afterglow-derived density normalization, we estimate the black-hole mass (see § 3 and equation 8),

$$M_\bullet \approx \left(6.55^{+3.51}_{-2.29}\right) \times 10^3\, n_0^{-2/3}\, c_{s,6}^2\, (1+\mathcal{M}^2)\, {\rm M_\odot}.$$

This is comfortably below the independent upper bound $M_\bullet \lesssim 5\times10^4\,{\rm M_\odot}$ inferred from the source-frame minimum variability time $t_{\rm MV,src} \approx 0.5$ s, and consistent with disruption of an MS star outside the event horizon. Within this framework:

(i) The soft X-ray pre-peak rising emission likely arises from a relativistic jet (as suggested by its $E_{\rm X,iso} \gtrsim 10^{52}$ erg, which is too large for isotropic emission with plausible efficiencies), during the circularization phase while an accretion disc builds up, leading to a gradual increase in the jet's power, Lorentz factor and degree of collimation. Its $\sim$ half-day (source frame) time-scale is naturally set by the sum of a circularization delay $t_{\rm circ} = f_{\rm circ}\, t_{\rm min}$ (with $f_{\rm circ} \sim$ few) and an accretion time $t_{\rm acc} \sim 10^{4.5}$ s at $R_{\rm circ} \sim 2r_p$ for $\alpha \sim 0.1$ and $h \sim 0.3-0.5$.

(ii) The multihour prompt γ-ray phase is naturally attributed to a fully developed, narrowly collimated ultrarelativistic jet, which emerges towards the end of the circularization stage when the accretion rate $\dot{M}_{\rm acc}$ is close to its peak value; its duration of order $t_{\rm min} + t_{\rm acc}$ matches the observed few-hour engine activity.

(iii) Intra-episode spacings of $\sim 10^3$ s are consistent with local viscous/thermal times at radii $r \sim$ (50-150) r_g. The afterglow fit requires a beaming-corrected kinetic energy $E_k \lesssim 10^{51}$ erg, which is achievable for jet efficiencies $\eta_j \sim 10^{-3}$–10^{-2} and accreted masses $M_{\rm acc} \sim \mathcal{O}(0.1-0.5)\,{\rm M_\odot}$.

5.2 A self-consistent physical picture

A coherent picture emerges in which a $\sim {\rm M_\odot}$ MS star is deeply disrupted ($\beta \gtrsim$ few) by an IMBH of $M_\bullet \sim 10^4\,{\rm M_\odot}$ embedded in warm ISM ($c_s \sim 10\ {\rm km\,s^{-1}}$) at an off-nuclear location. The environment interior to the capture radius, $R_{\rm B(HL)} \simeq 2GM_\bullet/[c_s^2(1+\mathcal{M}^2)]$, naturally provides $n(r) \propto r^{-3/2}$ as inferred from the afterglow modelling. The pre-peak rising X-ray emission is produced during the circularization process as an accretion disc starts to build-up, and the accretion rate $\dot{M}_{\rm acc}$ gradually increases along with the jet's degree of collimation and Lorentz factor. The main variable X-ray to gamma-ray emission arises once a powerful, narrowly collimated ultrarelativistic jet has formed and is powered by the near-peak accretion rate.

The main, variable X-ray to gamma-ray emission occurs when the jet is fully developed, ultrarelativistic and narrowly collimated, near the peak $\dot{M}_{\rm acc}$. Late-time, smoother emission is afterglow-dominated (FS), with a modest radio bump from the RS.

5.3 Alternative interpretations

Three families of alternatives remain:

(i) Ultralong collapsars or other stellar-engine models: such can potentially yield long durations, but are hard pressed to produce a ∼half-day gradually rising pre-peak soft X-ray emission, followed by a multihour peak, given that the jet needs to first bore its way through the progenitor massive star while its power is well below its peak value.

(ii) WD mTDEs: WD–IMBH tidal-disruption scenarios have been proposed for GRB 250702B and other ULGRBs (e.g. R. A. Eyles-Ferris et al. 2025; D. Y. Li et al. 2025) because WD structure can, in principle, provide short dynamical time-scales and strong gravity. However, a simple analytic treatment anchored to the observed properties of GRB 250702B shows that no self-consistent WD–IMBH configuration exists. Interpreting the intra-episode spacing $\Delta t_{\rm ep} \approx 2.8 \times 10^3$ s as an orbital or fallback clock should be compared with typical values of $t_{\rm min} \sim 20$–60 s, which are orders of magnitude shorter than the observed multihour prompt duration even when allowing for generous circularization delays. Conversely, choosing $t_{\rm min}$ large enough to power an hours-long engine would imply episode spacings far larger than observed. In addition, the cumulative mass that can be supplied by non-detonating partial-stripping passages over the observed time span is limited, so the beaming-corrected prompt energy can only be achieved for unrealistically narrow jets. Once basic detonation and ISCO constraints are also imposed, the allowed WD–IMBH parameter space for GRB 250702B essentially vanishes. We therefore regard a WD–IMBH origin as strongly disfavoured in comparison to the IMBH–MS mTDE scenario developed in this work, and refer the reader to P. Beniamini et al. (2025) for a complementary μTDE interpretation tailored to GRB 250702B.

(iii) micro-TDEs of an MS star by a SMBH: a detailed μTDE interpretation of GRB 250702B is presented in our companion paper (P. Beniamini et al. 2025). In brief, μTDEs (a stellar-mass BH/NS partially or fully disrupting an MS star) can naturally account for the sub-second variability and offer two viable routes to a day-scale pre-peak X-ray emission – the partial/repeating (dynamical) channel and the natal-kick (ballistic-delay) channel – both developed in P. Beniamini et al. (2025). Here, we note two points of tension that favour the IMBH mTDE picture for this event given the present afterglow data set: **(1)** the broad-band afterglow fit prefers a stratified external density with $n \propto r^{-k}$ and $k \approx 1.6$, suggestive of Bondi/BHL inflow on to an IMBH, whereas generic μTDE environments more often resemble uniform ISM or wind profiles unless special circumstances (ejecta/wind geometry) apply; and **(2)** the combination of extreme isotropic energy and multihour prompt duration can push μTDEs toward relatively narrow jets and/or high jet efficiencies. Both caveats are model-dependent and explored in P. Beniamini et al. (2025), which also lists observational discriminants (e.g. afterglow closure relations, very late radio calorimetry, pre-peak spectroscopy). We therefore regard μTDEs as a competitive alternative and refer the reader to P. Beniamini et al. (2025) for a comprehensive treatment tailored to GRB 250702B.

5.4 Model limitations and caveats

Our IMBH mass estimate is model-dependent: it assumes (a) that the blast wave is observed while still inside $R_{\rm B(HL)}$, (b) a quasi-steady Bondi/BHL profile, and (c) an external ISM characterized by (n_0, c_s) that are not directly measured. We did verify the self-consistency of (a) and (b) in § 3.1, but this still does not guarantee their validity. The circularization factor $f_{\rm circ}$ encapsulates complex GR hydrodynamics and may vary with β, BH spin, misalignment, and disc thickness; our choices ($f_{\rm circ} \sim$ few) are conservative but uncertain. Finally, the beaming factor and jet efficiency enter the prompt energy budget; both may evolve during the event.

5.5 Observational tests and predictions

The mTDE picture makes several falsifiable predictions:

- *Afterglow structure:* a transition from $k \approx 3/2$ to $k \approx 0$ is expected when the shock exits $R_{\rm BHL}$. This would produce a mild, achromatic light-curve flattening of $\Delta\alpha \approx 0.5$ for $\nu_m < \nu < \nu_c$ (PLS G, where PLS stands for the power-law segment of the afterglow synchrotron spectrum, and we are following the notations of J. Granot & R. Sari 2002) and a similar $\Delta\alpha \approx 0.5$ from $\alpha \approx 0$ to $\alpha \approx 0.5$ for $\nu < \mu_m < \nu_c$ (PLS D), but little change at $\nu > \max(\nu_m, \nu_c)$ (PLS H). Following the discussion at the end of § 3.1, this transition might potentially be expected at approximately $t_B \sim 10^2$ days or so. Very late-time monitoring could reveal this transition.
- *Jet geometry:* a jet break may be very gradual in a stratified medium; deep late-time radio/X-ray observations may constrain θ_j via calorimetry, improving the beaming-corrected energy.
- *VLBI size and motion:* high-resolution VLBI observations in the radio can test for modest apparent expansion speeds and constrain the external density normalization independently of the SED fit.
- *Host environment:* off-nuclear, dusty star-forming regions or star clusters at several kpc are natural locales for IMBHs; deep imaging/spectroscopy may reveal an associated compact stellar system.

5.6 Event rates and broader implications

Accounting for selection biases, ULGRBs constitute a small fraction of GRBs, with an intrinsic rate plausibly ∼1–20 $\rm Gpc^{-3}\,yr^{-1}$ after beaming corrections. Current estimates for IMBH TDEs in clusters and off-nuclear environments span ∼0.1–10 $\rm Gpc^{-3}\,yr^{-1}$ with large uncertainties. If only a minority launch jets ($f_{\rm j} \sim 10^{-1.5}$) and are beamed towards us, the observable rate becomes comparable to the detected ULGRB rate, suggesting that MS mTDEs could account for at least a sub-set of ULGRBs. Future wide-field, high-duty-cycle X-ray monitors paired with prompt radio follow-up will be key to building statistics.

5.7 Outlook

Several improvements can sharpen the mTDE interpretation: (i) late-time radio calorimetry and VLBI size constraints; (ii) deeper X-ray monitoring to search for the predicted density-profile transition; (iii) polarimetry of the afterglow (jet magnetization); (iv) host-environment studies to identify a bound star cluster or dense association; and (v) detailed GRMHD simulations tailored to $M_\bullet \sim 10^4\,{\rm M}_\odot$ with realistic debris injection and BHL inflow. If confirmed, GRB 250702B would establish IMBH mTDEs as a natural channel for ultralong gamma-ray transients and provide a new probe of wandering black holes and their environments at cosmological distances.

In summary, the MS mTDE scenario around an IMBH of $M_\bullet \sim 10^4\,{\rm M}_\odot$ self-consistently explains the half-day scale pre-peak X-

ray emission, the multi-hour prompt X-ray to gamma-ray emission, the rapid variability, and the afterglow's $n(r) \propto r^{-3/2}$ profile. While alternative models remain possible, the specific, testable predictions above offer a clear path to validating or refuting this interpretation with continued observations.

ACKNOWLEDGEMENTS

We thank Eric Coughlin for useful discussions. PB's work was funded by a grant (no. 2020747) from the United States-Israel Binational Science Foundation (BSF), Jerusalem, Israel and by a grant (no. 1649/23) from the Israel Science Foundation. BO acknowledges support from the McWilliams Fellowship in the McWilliams Center for Cosmology and Astrophysics at Carnegie Mellon University.

This work used resources on the Vera Cluster at the Pittsburgh Supercomputing Center (PSC). Vera is a dedicated cluster for the McWilliams Center for Cosmology and Astrophysics at Carnegie Mellon University. We thank the PSC staff for their support of the Vera Cluster.

The scientific results reported in this article are based on observations made by the *Chandra* X-ray Observatory. This research has made use of software provided by the *Chandra* X-ray Center (CXC) in the application package CIAO. This work made use of data supplied by the UK *Swift* Science Data Centre at the University of Leicester. This research has made use of the XRT Data Analysis Software (XRTDAS) developed under the responsibility of the ASI Science Data Center (ASDC), Italy. This research has made use of data and/or software provided by the High Energy Astrophysics Science Archive Research Center (HEASARC), which is a service of the Astrophysics Science Division at NASA/GSFC.

DATA AVAILABILITY

No data base was used in this work.

REFERENCES

Alexander K. D. et al., 2025, GRB Coordinates Network, 41059, 1
Atri P., Rhodes L., Fender R., Hughes A., Motta S., XKAT Collaboration, 2025, GRB Coordinates Network, 41054, 1
Balasubramanian A. et al., 2025, GRB Coordinates Network, 41145, 1
Beniamini P., Granot J., Gill R., 2020, MNRAS, 493, 3521
Beniamini P., Gill R., Granot J., 2022, MNRAS, 515, 555
Beniamini P., Perets H. B., Granot J., 2026, The Open Journal of Astrophysics, 9
Blandford R., McKee C., 1976, Phys. Fluids, 19, 1130
Blondin J. M., Raymer E., 2012, ApJ, 752, 30
Bobrick A., Davies M. B., Perets H. B., 2025, MNRAS, 544, 3601
Boër M., Gendre B., Stratta G., 2015, ApJ, 800, 16
Carney J. et al., 2025, ApJ, 994, L46
Cheng H. Q. et al., 2025, GRB Coordinates Network, 40906, 1
Coughlin E. R., Nixon C., 2015, ApJ, 808, L11
Coughlin E. R., Nixon C. J., 2019, ApJ, 883, L17
De Colle F., Ramirez-Ruiz E., Granot J., Lopez-Camara D., 2012, ApJ, 751, 57
de Wet S. et al., 2023, A&A, 677, A32
Eichler D., Livio M., Piran T., Schramm D. N., 1989, Nature, 340, 126
Eyles-Ferris R. A. et al., 2026, MNRAS, 546, 1
Eyles-Ferris R. A. J. et al., 2025, GRB Coordinates Network, 41767, 1
Fragione G., Leigh N. W. C., Ginsburg I., Kocsis B., 2018, ApJ, 867, 119
Frederiks D., Lysenko A., Ridnaia A., Svinkin D., Tsvetkova A., Ulanov M., Cline T., Konus-Wind Team, 2025, GRB Coordinates Network, 40914, 1
Freire P. C., Kramer M., Lyne A. G., Camilo F., Manchester R. N., D'Amico N., 2001, ApJ, 557, L105
Gehrels N. et al., 2004, ApJ, 611, 1005
Gendre B., 2025, Galaxies, 13, 7
Gendre B. et al., 2013, ApJ, 766, 30
Gill R., Granot J., 2018, MNRAS, 478, 4128
Gill R., Granot J., 2023, MNRAS, 524, L78
Gompertz B. P., Fruchter A. S., Pe'er A., 2018, ApJ, 866, 162
Gompertz B. P. et al., 2026, ApJ, 997, L4
Granot J., 2005, ApJ, 631, 1022
Granot J., 2007, Rev. Mex. Astron. Astrofis, 27, 140
Granot J., 2012, MNRAS, 421, 2442
Granot J., Sari R., 2002, ApJ, 568, 820
Granot J. et al., 2006, ApJ, 638, 391
Greene J. E., Strader J., Ho L. C., 2020, ARA&A, 58, 257
Greiner J. et al., 2015, Nature, 523, 189
Grollimund N., Corbel S., Coleiro A., Cangemi F., Rodriguez J., 2025, GRB Coordinates Network, 41147, 1
Guillochon J., Ramirez-Ruiz E., 2013, ApJ, 767, 25
Hayasaki K., Stone N., Loeb A., 2016, MNRAS, 461, 3760
Kawakubo Y. et al., 2025, GRB Coordinates Network, 40910, 1
Kennea J. A., Siegel M. H., Evans P. A., Page K. L., O'Connor B., Swift Team, 2025, GRB Coordinates Network, 40919, 1
Kobayashi S., Sari R., 2000, ApJ, 542, 819
Kobayashi S., Zhang B., 2003, ApJ, 597, 455
Kouveliotou C., Meegan C. A., Fishman G. J., Bhat N. P., Briggs M. S., Koshut T. M., Paciesas W. S., Pendleton G. N., 1993, ApJ, 413, L101
Kouveliotou C. et al., 2013, ApJ, 779, L1
Kremer K., Mockler B., Piro A. L., Lombardi J. C., 2023, MNRAS, 524, 6358
Lan G.-X., Zeng H.-D., Wei J.-J., Wu X.-F., 2019, MNRAS, 488, 4607
Levan A. J. et al., 2014, ApJ, 781, 13
Levan A. J. et al., 2025, ApJ, 990, L28
Li D. Y., Yang J., Zhang W. D., 2025, preprint (arXiv:2509.25877)
Liang E.-W. et al., 2013, ApJ, 774, 13
Lien A. et al., 2016, ApJ, 829, 7
Livio M., Soker N., de Kool M., Savonije G. J., 1986, MNRAS, 222, 235
Lodato G., King A. R., Pringle J. E., 2009, MNRAS, 392, 332
Lu W., Bonnerot C., 2020, MNRAS, 492, 686
McDonald I., Zijlstra A. A., 2015, MNRAS, 446, 2226
McKinney J. C., Tchekhovskoy A., Blandford R. D., 2012, MNRAS, 423, 3083
Nakar E., Granot J., 2007, MNRAS, 380, 1744
Nava L., Sironi L., Ghisellini G., Celotti A., Ghirlanda G., 2013, MNRAS, 433, 2107
Neights E. et al., 2026, MNRAS, 545, 1
Neights E., Roberts O. J., Burns E., Veres P., Fermi-GBM Team, 2025b, GRB Coordinates Network, 40891, 1
Neights E., Roberts O. J., Burns E., Veres P., Bissaldi E., , 2025c, GRB Coordinates Network, 40931, 1
O'Connor B. et al., 2025, ApJ, 994, L17
Perets H. B., Li Z., Lombardi J. C., Jr, Milcarek S. R., Jr, 2016, ApJ, 823, 113
Rossi E. M., Stone N. C., Law-Smith J. A. P., Macleod M., Lodato G., Dai J. L., Mandel I., 2021, Space Sci. Rev., 217, 40
Rossi J., Servin J., Kesden M., 2021, Phys. Rev. D, 104, 103019
Rozner M., Trani A. A., Samsing J., Perets H. B., 2025, MNRAS, 537, 1220
Sari R., Piran T., 1995, ApJ, 455, L143
Sari R., Piran T., Narayan R., 1998, ApJ, 497, L17
Schlafly E. F., Finkbeiner D. P., 2011, ApJ, 737, 103
Sfaradi A. I. et al., 2025, GRB Coordinates Network, 41053, 1
Steinberg E., Stone N. C., 2024, Nature, 625, 463
Stone N., Sari R., Loeb A., 2013, MNRAS, 435, 1809

Stone N. C., Metzger B. D., 2016, MNRAS, 455, 859
Tchekhovskoy A., Narayan R., McKinney J. C., 2011, MNRAS, 418, L79
Tchekhovskoy A., McKinney J. C., Narayan R., 2012, J. Phys. Conf. Ser., 372, 012040
Tetarenko A. J., Bright J., Bower G., Graves S., 2025, GRB Coordinates Network, 41061, 1
Tikhomirova Y. Y., Stern B. E., 2005, Astron. Lett., 31, 291
Vynatheya P., Ryu T., Pakmor R., de Mink S. E., Perets H. B., 2024, A&A, 685, A45
Wanderman D., Piran T., 2010, MNRAS, 406, 1944
Wang Y.-H., Perna R., Armitage P. J., 2021, MNRAS, 503, 6005
Wei J. et al., 2016, preprint (arXiv:1610.06892)
Wijers R. A. M. J., 2001, in Costa E., Frontera F., Hjorth J. eds, Gamma-ray Bursts in the Afterglow Era. Springer-Verlag, Berlin, p. 306
Woosley S. E., 1993, ApJ, 405, 273
Wu Z.-F., Damoulakis M., Beniamini P., Giannios D., 2025, ApJ, 980, L28
Xin C., Haiman Z., Perna R., Wang Y., Ryu T., 2024, ApJ, 961, 149
Xu W., Stone J. M., 2019, MNRAS, 488, 5162
Zhou Q.-Q., Yi S.-X., Huang X.-L., Zhong S.-Q., Zou Y.-C., Tang Q.-W., Chen Z.-F., 2020, Int. J. Mod. Phys. D, 29, 2050043

APPENDIX A: AFTERGLOW FIT POSTERIOR DISTRIBUTIONS

In Fig. A1, we present the model parameter posteriors from our fit to the afterglow data.

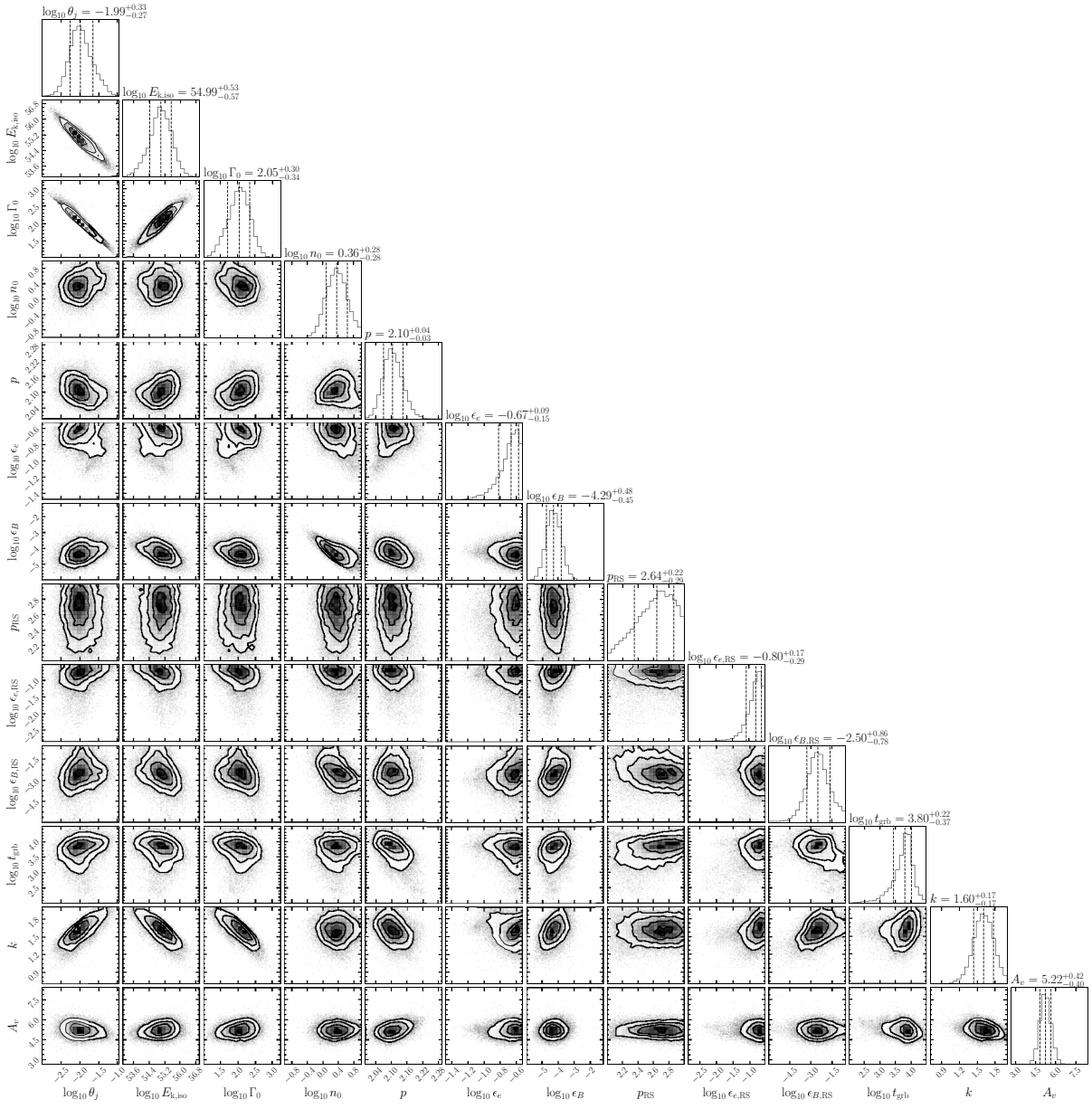

Figure A1. Model parameter posterior distributions obtained from an MCMC fit to the GRB 250702B multiwavelength afterglow data using the afterglow model of R. Gill & J. Granot (2023).

This paper has been typeset from a TEX/LATEX file prepared by the author.